ACS APPLIED MATERIALS & INTERFACES
Research Article
www.acsami.org

Cupreous Complex-Loaded Chitosan Nanoparticles for Photothermal Therapy and Chemotherapy of Oral Epithelial Carcinoma

Min Lin,[†] Dandan Wang,[‡] Shuwei Liu,[†] Tingting Huang,[†] Bin Sun,[‡] Yan Cui,[‡] Daqi Zhang,[*,§] Hongchen Sun,[*,‡] Hao Zhang,[*,†] Hui Sun,[§] and Bai Yang[†]

[†]State Key Laboratory of Supramolecular Structure and Materials, College of Chemistry, [‡]Department of Oral Pathology, School and Hospital of Stomatology, and [§]Department of Thyroid Surgery, China-Japan Union Hospital, Jilin University, Changchun 130012, P. R. China

Supporting Information

ABSTRACT: Electron transition materials on the basis of transition metal ions usually possess higher photothermal transduction efficiency but lower extinction ability, which have not been considered as efficient photothermal agents for therapeutic applications. In this work, we demonstrate a facile and feasible approach for enhancing 808 nm photothermal conversion effect of d orbits transition Cu(II) ions by forming Cu-carboxylate complexes. The coordination with carboxylate groups greatly enlarges the splitting energy gap of Cu(II) and the capability of electron transition, thus enhancing the extinction ability in near-infrared region. The cupreous complexes are further loaded in biocompatible and biodegradable polymer nanoparticles (NPs) of chitosan to temporarily lower the toxicity, which allows the photothermal therapy of human oral epithelial carcinoma (KB) cells in vitro and KB tumors in vivo. Animal experiments indicate the photothermal tumor inhibition rate of 100%. In addition, the gradual degradation of chitosan NPs leads to the release of cupreous complexes, thus exhibiting additional chemotherapeutic behavior in KB tumor treatment. Onefold chemotherapy experiments indicate the tumor inhibition rate of 93.1%. The combination of photothermal therapy and chemotherapy of cupreous complex-loaded chitosan NPs indicates the possibility of inhibiting tumor recurrence.

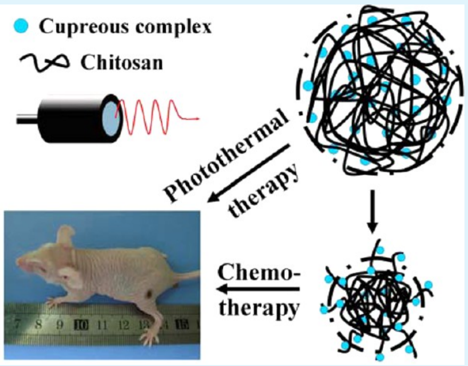

KEYWORDS: *cupreous complexes, chitosan, nanocomposites, photothermal therapy, chemotherapy*

INTRODUCTION

Photothermal therapy, aimed at ablating malignant tissue noninvasively by heating the tissue locally above 43 °C on the basis of the photothermal effect of nanomaterials, has attracted increasing attention in the past five years.[1−3] As the heat generators, nanomaterials can absorb and convert near-infrared (NIR) light into heat energy under external laser stimulating.[4−6] To achieve better penetration depth and limited damage to healthy organs and tissues, the NIR lasers ranging from 650 to 980 nm are usually adopted as the energy source for lowering the self-absorption of organism.[7−10] Despite the advantages of photothermal therapy against traditional chemotherapy and radiotherapy, photothermal therapy alone still faces the risk of tumor recurrence caused by invasiveness.[11] Consequently, photothermal therapy is considered to combine with other treatment.[12−15] For example, chemotherapy has been widely applied in clinical treatment of tumors, but the anticancer drugs may cause severe side effects due to the indiscriminate damage both on healthy and cancerous cells. If the drugs can target specific cancerous area or be released inner tumors, the delivery of high concentration of drugs locally will greatly improve the treatment effect. Except for commercially available anticancer drugs, the materials with high cytotoxicity may also be adopted as anticancer agents if they do not generate any systemic toxicity. Therefore, photothermal therapy is usually combined with chemotherapy, named thermo-chemotherapy, to achieve the additional release of chemotherapeutic drugs in a controlled manner through light and/or heat stimulus.[16−19] This method greatly increases the concentration of drugs in the targeted cancerous area, thus overcoming the safe dose limitation of drugs in the normal tissue. The synergistic effect of targeted heat delivery and controlled drug release has shown better efficacy in tumor treatment than photothermal therapy and chemotherapy alone, though the anticancer drugs are expensive and the loading of them in photothermal nanomaterials is still complex. Nevertheless, the capability of chemotherapeutic drugs to continuously destroy the remaining living cancerous cells after photothermal therapy makes thermo-chemotherapy a competitive candidate to simultaneously perform noninvasive tumor ablation and reduce the risk of tumor recurrence.[20,21]

As the source to convert NIR irradiation into heat, photothermal nanomaterials play the key role in both photothermal therapy and thermo-chemotherapy, which greatly

Received: June 30, 2015
Accepted: September 4, 2015
Published: September 4, 2015

DOI: 10.1021/acsami.5b05866
ACS Appl. Mater. Interfaces 2015, 7, 20801−20812

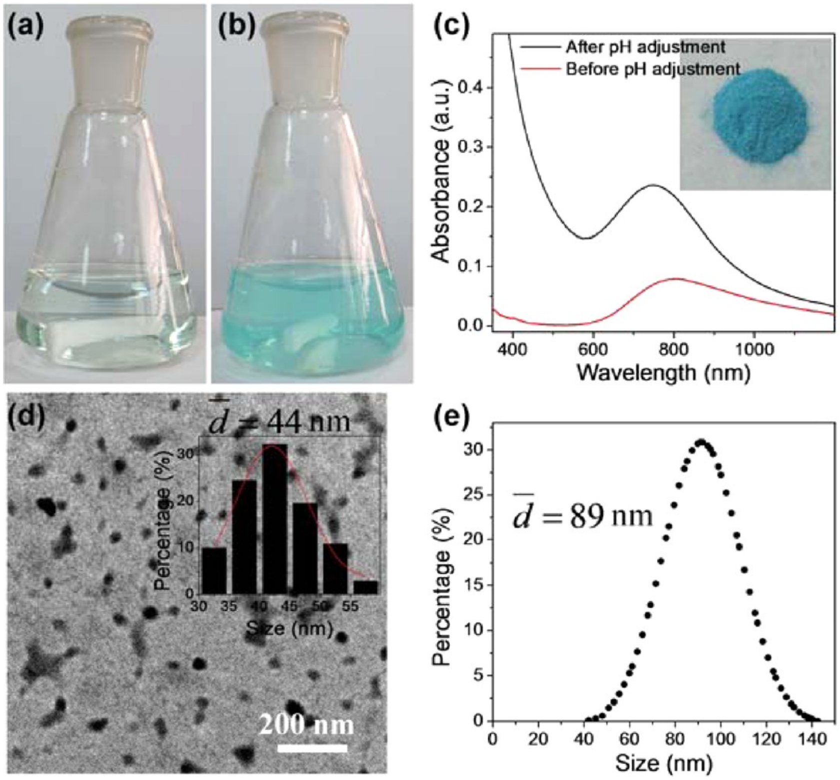

Figure 1. Characterization of CuCC NPs that are prepared by adjusting the pH of $CuCl_2$, citrate acid, and chitosan mixtures to 3.53 ± 0.5. (a, b) Photographs of the mixtures before (a) and after (b) pH adjustment. (c) The corresponding absorption spectra. (inset) Photograph of CuCC NPs powder. (d, e) TEM image (d) and DLS size distribution (e) of CuCC NPs. (inset) TEM size distribution by counting 300 NPs, which accords with Gauss distribution.

influence the therapeutic procedure and activity.[22−25] So far, the most studied nanomaterials include plasmonic materials and electronic transition materials, which generate heat on the basis of electrons oscillation and transition, respectively.[26,27] Plasmonic nanomaterials, mainly referring to noble metals, possess synchronized oscillation of electrons from the conduction-band of metals in the presence of light.[28] Thus, they can strongly absorb and scatter light around their resonant wavelength that greatly depends on their size, shape, and morphology.[29,30] One of the most tested examples is gold-based nanomaterials.[31] Gold nanorods,[32,33] nanoshells,[34,35] nanostars,[36,37] and nanocages[38] have been applied for treating tumor models in vivo, including photothermal ablation, targeted drug delivery, controlled drug release, and so forth.[39] Although their strong cross-section extinction ability can generate adequate heat, their metallic property leads to a great tendency to scatter light, thus lowering the photothermal transduction efficiency.[2] In addition, although the morphology control of noble metal nanomaterials is feasible in laboratory scale, larger-scale preparation of nonspherical nanomaterials is still challenging.[40,41]

Thanks to the diversity of nonmetallic materials, electronic transition materials are also tested as photothermal agents.[42] The capability of photothermal transduction is led from the electrons transition between molecular/atomic orbital energy levels, where the energy gap matches the light in NIR region.[27] In addition, electronic transition materials usually possess improved potentials in biocompatibility, easy surface modification, repeatable preparation, high photothermal transduction efficiency, and low cost.[43−47] These advantages make electronic transition materials as the alternatives to plasmonic materials. Until now, molecular orbital transition takes up the most of electronic transition materials, such as organic dyes,[42] polymer nanoparticles (NPs),[27,48] carbon-based nanomaterials,[49,50] and so forth. Atomic orbital transition has been seldom reported, because the energy gap only matches the light in ultraviolet and visible region.[51,52] An exception is cupreous complexes. The d orbits of Cu(II) can split under the ligand field with specific geometry, thus generating degenerate orbits.[53] For example, according to the symmetric match between d orbits and octahedral ligand field, six-coordinative Cu(II) has a d^9 electronic configuration, and three of the electrons are in the two higher degenerate e_g orbits, while the others are in the three lower degenerate t_{2g} orbits.[53,54] The energy gap between e_g and t_{2g} is called splitting energy, which may match the energy of NIR region as proper ligand field forms. This shows the possibility of electronic transition materials in atomic orbital energy levels as photothermal agents. Cupreous complexes are also toxic. If the toxicity is well manipulated, the nanomaterials will simultaneously possess photothermal therapeutic and chemotherapeutic activities.

Polymer envelopment has been proved as an efficient approach for improving the stability and even enhancing the functionalities of nanometer-sized building blocks.[55,56] With respect to bioapplicable materials, the envelopment of inorganic nanomaterials using biocompatible polymers further lowers the toxicity.[57,58] Among various biocompatible polymers, chitosan is one of the most tested polymers for loading drugs because of the good biocompatibility.[59] The biodegradable property of chitosan also makes it as commercially used sustained drug release matrix. This reveals that if toxic cupreous complexes are loaded in chitosan, the resulting composites will exhibit

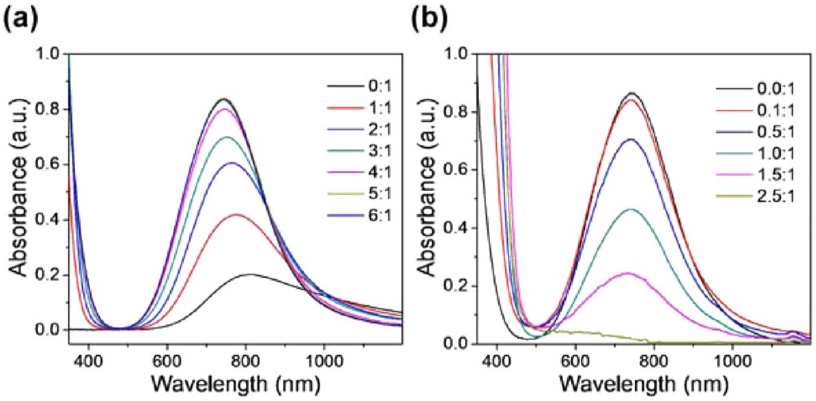

Figure 2. (a) The absorption spectra of cupreous complexes as increasing carboxylate-to-Cu(II) molar ratio from 0/1 to 6/1 (each sodium citrate possesses three carboxylate groups). (b) The absorption spectra of cupreous complexes measured after gradually replacing sodium citrate with MPA. The initial carboxylate-to-Cu(II) molar ratio in the complexes is 6, whereas the MPA-to-Cu(II) ratio increase from 0/1 to 2.5/1.

chemotherapeutic behavior through the gradual degradation of chitosan. However, the compatibility of chitosan with Cu(II) ions is in general poor. Additional connections must be brought for preparing Cu(II)-loaded chitosan NPs. In this context, chitosan will protonate in water under acidic range. The protonated chitosan can further connect with negatively charged molecules through electrostatic attraction. If the structure of cupreous complexes is well-designed, Cu(II)-loaded chitosan NPs with improved photothermal therapeutic and chemotherapeutic behavior will be fabricated.

In this work, we demonstrate a facile and low-cost approach for preparing cupreous complexes-loaded chitosan (CuCC) NPs. Citric acid is adopted as the bridge for connecting Cu(II) and chitosan matrix. The formation of Cu(II)-citrate complexes greatly promotes the d orbits splitting, thus enhancing the extinction ability and photothermal performance of Cu(II). The improved biocompatibility and stability of cupreous complexes allow the photothermal therapy of human oral epithelial carcinoma (KB) cells in vitro and KB tumors in vivo. Moreover, the gradual degradation of chitosan NPs leads to additional chemotherapy through the release of toxic Cu(II).

■ RESULTS AND DISCUSSION

CuCC NPs are prepared by facilely adjusting the pH of the aqueous mixtures of citric acid, $CuCl_2$, and chitosan to 3.53 ± 0.5 (Figure 1a,b), which allows the low-cost and large-scale preparation. Before pH adjustment, citric acid accelerates chitosan dispersion in water by promoting chitosan protonation. Cu(II) ions can coordinate with the carboxylate groups generated from citric acid deprotonation,[53] thus in return promoting the dissolution of citric acid and subsequently chitosan. The resulting mixture shows a weak absorption peak around 820 nm (Figure 1c). Further pH adjustment to 3.53 ± 0.5 leads to the variation of solution color in cyan (Figure 1b). Under transmission electron microscopy (TEM), quasi-spherical NPs with an average diameter of 44 ± 14 nm are observed (Figure 1d). Dynamic light scattering (DLS) measurement exhibits the average diameter of 89 nm (Figure 1e), which is larger than TEM observation. This is attributed to the dried structures in TEM characterization. The formation of CuCC NPs mainly results from the linkage of citric acid with both Cu(II) and chitosan. In this context, the deprotonated citric acids partially coordinate with Cu(II), while the remaining ones link with protonated chitosan through charge−charge interaction. FTIR spectra confirm this consideration, which show the decrease of −COOH peak at 1720 cm^{-1} and the increase of $-COO^-$ peak at 1520 cm^{-1} (Figure S1).

In comparison to the primary mixture, the CuCC NPs exhibit enhanced extinction ability in NIR region (Figure 1c). The slightly blue shift of absorption peak results from the formation of ligand field, which increases the splitting energy of d orbits transition in Cu(II).[53] For better understanding, the coordination interaction between sodium citrate and $CuCl_2$ is studied (Figure 2a). As increasing the molar ratio of carboxylate group to Cu(II) from 1:1 to 6:1, blue shift and intensity increase are observed in the absorption spectra. When the ratio is higher than 5:1, the intensity and position of absorption spectra are almost fixed, because each Cu(II) ion can only coordinate with four carboxylate groups at most. Since citric acid is weak acid, sodium citrate also hydrolyzes in water, which explains why the citrate-to-$CuCl_2$ feed ratio is slightly higher than the real coordination number. The aforementioned result indicates that the increase of absorption intensity of CuCC NPs may relate to the alteration of Cu(II) coordination number. When dissolved in water, each Cu(II) ion coordinates with six H_2O to form a octahedral structure, namely, $[Cu(H_2O)_6]^{2+}$.[54] The octahedral ligand field leads to the weak absorption around 830 nm. With the addition of sodium citrate, the H_2O molecules coordinated with Cu(II) are gradually replaced by carboxylate groups because of the strong Cu-carboxylate coordination. This disturbs the original octahedral ligand fields. As one carboxylate occupies a coordinate position, the energy of degenerate d_{z^2} orbit will further elevate. In another word, e_g energy level splits into higher level of d_{z^2} and relatively lower level of $d_{x^2-y^2}$. Therefore, the splitting energy becomes higher and exhibits blue shift in the absorption peak.[54] Because of the stronger electron donating ability of the oxygen in carboxylate group than that in water, an intensity increase of absorption spectra is observed. When more carboxylates coordinate with Cu(II), e_g level continues to split, and the energy of $d_{z^2}/d_{x^2-y^2}$ further improves according to the symmetry of ligand field.[54] As a result, the absorption peak exhibits continuous blue shift and intensity increase. This consideration is firmly proved when sodium citrate is substituted with sulfydryl (Figure 2b). Sulfydryl possesses higher coordinative ability with Cu(II), thus generating higher splitting energy and the consequent blue shift in absorption spectra. However, the electron donating ability of sulfydryl is so well that Cu catches the electrons by fulfilling the d^{10} orbits, which suppresses the d−d electron

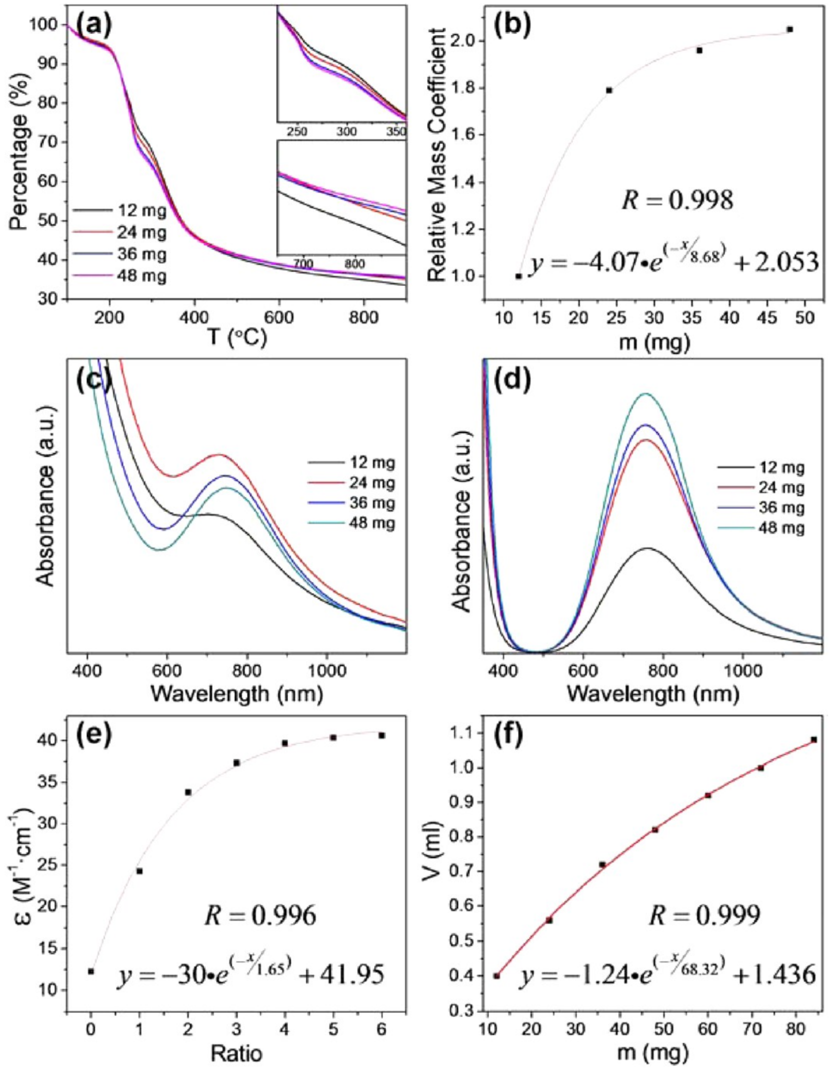

Figure 3. (a) TGA curves of the CuCC NPs that are prepared by altering the feeding amount of $CuCl_2$. (insets) The partially enlarged view at the temperature range of 240−370 and above 650 °C, which represent the decomposition of citric acid, chitosan, and the preservation. (b) The relation between Cu content in CuCC NPs (relative mass coefficient) and the feeding amount of $CuCl_2$, which is calculated from TGA data. (c, d) Comparison of the absorption spectra of the mixtures with (c) and without (d) chitosan after pH adjustment to 3.53 ± 0.5. The feeding amount of $CuCl_2$ is altered from 12 to 48 mg. (e) The molar absorption coefficient of cupreous complexes at 808 nm vs carboxylate-to-Cu(II) feed ratio. (f) The consumption of NaOH vs the feeding amount of $CuCl_2$.

transition and lowers the absorption intensity. In all, the increased extinction ability of cupreous complexes is attributed to electron−electron transition between the splitting d orbits, which is induced by the coordination of Cu(II) with deprotonated citric acid.

The photothermal performance of CuCC NPs can be represented by two factors, molar absorption coefficient (ε)/molar extinction coefficient (Q_{ext}) and photothermal transduction efficiency (η).[2] These two parameters concern with the capability of absorbing light and converting light into heat, respectively. Experimental results indicate that the ε of $[Cu(H_2O)_6]^{2+}$ complexes at 808 nm is 12.3 M^{-1} cm^{-1}, while ε increases to 40.6 M^{-1} cm^{-1} after forming cupreous complexes (Figure 3e). As to CuCC NPs, the calculated Q_{ext} is ~4.7 × 10^7 $M^{-1}\cdot cm^{-1}$ (Calculation S1). It is lower than plasmonic nanomaterials such as Au nanorods and CuS nanoplates (1 × 10^8 to ca. 1 × 10^9 $M^{-1}\cdot cm^{-1}$), but higher than that of carbon nanotubes (~1 × 10^6 $M^{-1}\cdot cm^{-1}$). In addition, the η of cupreous complexes at 808 nm is evaluated by eq 1.[2]

$$\eta = \frac{hS(T_{max} - T_{surr}) - Q_0}{P(1 - 10^{-A_{808}})} \tag{1}$$

where h is heat transfer coefficient, S is the contacting area between container and environment, T_{surr} is the ambient temperature, Q_0 represents the heat generated by water and quartz cell under laser irradiation, P is incident laser power, and A_{808} is the absorption intensity of cupreous complexes at 808 nm. To calculate η, the heat transfer coefficient h should be known. According to our previous work, h is determined under the heat diffusion process. The lasting temperature decrease is recorded at fixed time intervals (Figure S2a). We replace the ($T - T_{surr}$) with θ and make a linear fit of time (t) and $-\ln(\theta/T_{max})$ (Figure S2b), where h can be calculated from the slope of fitted eq 2:

$$t = \frac{\sum m_i C_{p,i}}{hS}(-\ln \theta/T_{max}) + b \tag{2}$$

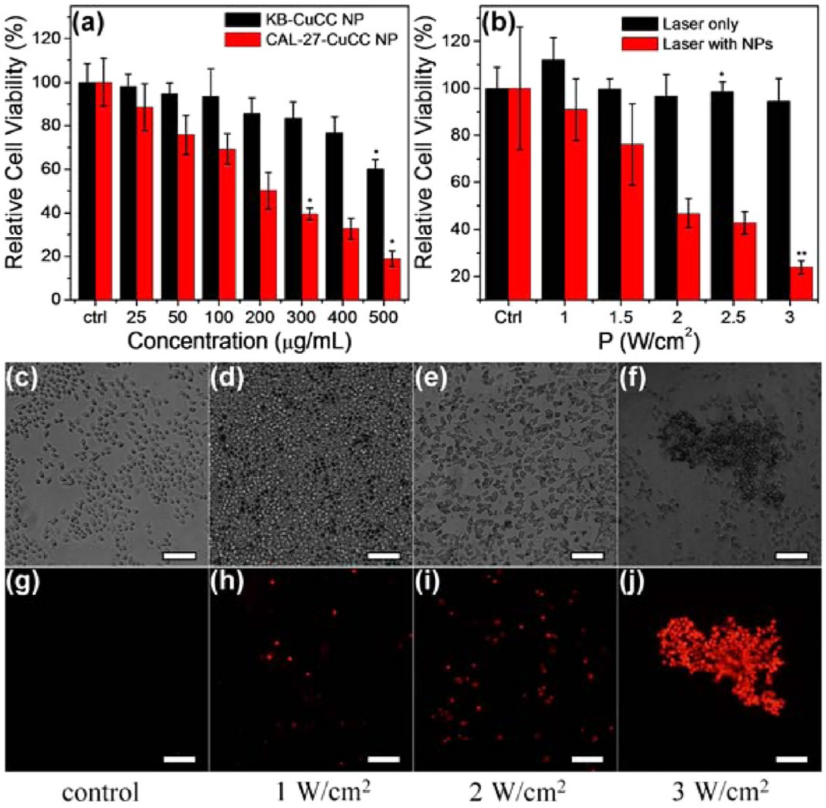

Figure 4. Photothermal therapy of KB cells in vitro. (a) KB and CAL-27 cells are incubated with CuCC NPs for 24 h, and cell viability is estimated through standard MTT assay. (b) The KB cells are incubated with and without 100 μg/mL CuCC NPs for 4 h, and then they are irradiated by an 808 nm laser with the power density of 1, 1.5, 2, 2.5, and 3 W/cm^2 for 10 min. Bright field (c−f) and fluorescent (g−j) images of KB cells after irradiated by an 808 nm laser with the power density of 0 (c, g), 1 (d, h), 2 (e, i), and 3 (f, j) W/cm^2 for 10 min. The scale bar is 50 μm. Data are shown as the means ± standard error of the means, * $p < 0.05$ and ** $p < 0.01$.

where m_i and $C_{p,i}$ are the mass and heat capacity of the irradiated system including water, cell, and cupreous complexes. As time constant $\Sigma m_i C_{p,i}/hS$ equals 414.1 s, the h is determined to be 32.88 W m^{-1} K^{-1}. Besides, the m_i is 2 and 5.827 g, while the $C_{p,i}$ is 4.2 J g^{-1} K^{-1} and 0.892 J g^{-1} K^{-1} for water and quartz cell, respectively. Therefore, the calculated η at 808 nm is 54.1, 60.0, 60.2, and 60.3% for the cupreous complexes with carboxylate-to-Cu(II) molar ratio of 1/1, 2/1, 3/1, and 4/1, respectively.

Note that the photothermal performance is fully contributed from cupreous complexes, whereas chitosan has no photothermal contribution. It is thought to optimize the photothermal performance of CuCC NPs by increasing the loaded cupreous complexes, which is studied by thermogravimetric analysis (TGA). TGA data indicate two weight loss regions at 200−270 and 270−400 °C, corresponding to the decomposition of citric acid and chitosan (Figures 3a and S3). As increasing the feeding amount of CuCl$_2$, the as-prepared CuCC NPs indicate a higher content of chitosan and Cu (Figure 3a). We fit the relative mass coefficient (M_r) with the feeding amount of CuCl$_2$ (m) as shown in eq 3 (Figure 3b):

$$M_r = -4.07{*}e^{(-m/8.68)} + 2.053 \quad (3)$$

Thus, the absorption intensity of CuCC NPs prepared with different CuCl$_2$ feeding amount is corrected by M_r. After M_r correction, it is found that when the amounts of chitosan and citric acid are fixed, the corrected absorption spectrum reaches maximum at the CuCl$_2$ feeding amount of 24 mg (Figure 3c). In comparison, the absorption intensity of Cu(II)-citrate complexes in the absence of chitosan keeps increasing with the increase of CuCl$_2$ feeding amount (Figure 3d). It means that before 24 mg, the increase of absorbance is led from the increase of cupreous complexes loaded in CuCC NPs. The afterward decrease is attributed to the reduced coordination number of Cu(II), which greatly influences the extinction ability of cupreous complexes (Figure 3e). It should be mentioned that more NaOH is consumed in preparing CuCC NPs as increasing Cu(II) dose (Figure 3f), implying that more carboxylate groups are generated by Cu(II)-carboxylate coordination. The aforementioned results reveal that excessive carboxylate groups are not helpful in enhancing NPs extinction, because of the competitive coordination equilibrium with Cu(II). Excessive Cu(II) in return decreases the coordination number, and therewith lowers the absorption intensity in NIR region.

Both CuCC NPs and cupreous complexes can greatly increase the system temperature under 808 nm laser irradiation (Figure S4). Setting the laser power at 3.5 W/cm^2, the temperature of 2 mL of 5 mg/mL CuCC NPs aqueous solution elevates 33.4 °C after 15 min of laser irradiation, while the solution of 1.2 mg/mL CuCC NPs only elevates 13.2 °C (Figure S4a). This is attributed to the collective heating effect of the solution with high concentration.[5] More irradiation is absorbed and converted into heat energy with high concentration photothermal agents. Besides, the increase of power density and irradiation duration also elevates the temperature significantly, because high dose of irradiation is imposed (Figure S4b). The same trend is observed for

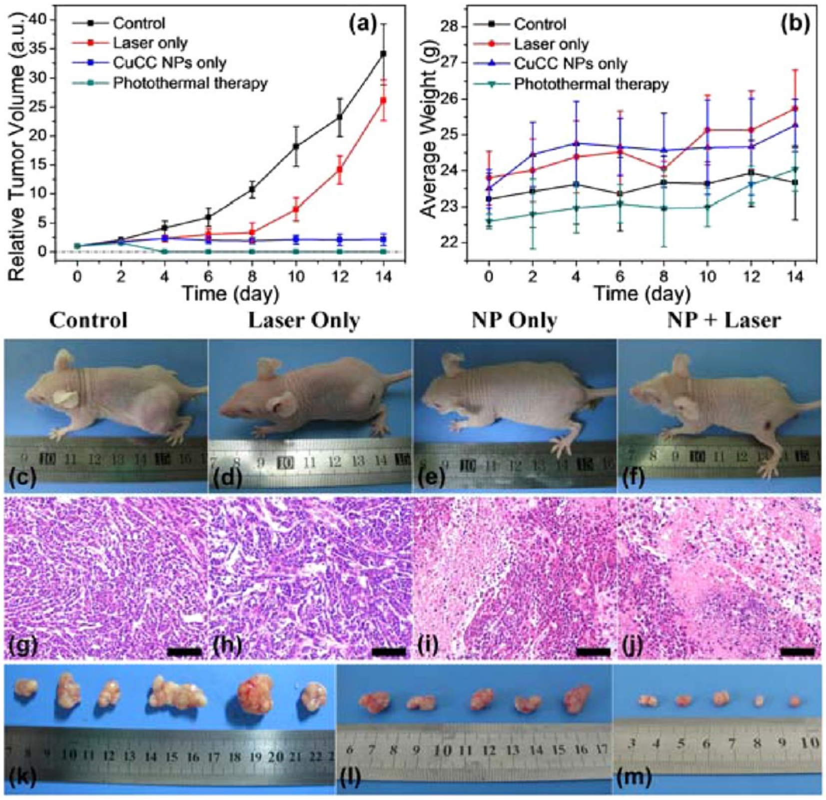

Figure 5. In vivo photothermal therapy. The mice are divided into four groups, namely, control group (c, g, k), laser only group (d, h, l), NP only group (e, i, m), and photothermal therapy group (f, j). Relative tumor volume (a) growing trend and average body weight (b) for each group. Photographs of typical mouse bearing tumor model (c−f), H&E staining of tumor slices (g−j), and tumors (k−m) taken from them in each group in the 16th day after NP injection. H&E staining of tumor slice for photothermal therapy group is performed immediately after laser irradiation. The average tumor weight is 1.24, 0.75, 0.08, and 0 g for each group, respectively. The dose of injected CuCC NPs is 100 μg in 50 μL saline per mouse. The laser power density is set at 0.33 W/cm^2. The scale bar in g−j represents 50 μm.

cupreous complexes (Figure S4c,d). In addition, the photothermal performance of cupreous complexes enhances as increasing the coordination number of Cu(II). As irradiated by an 808 nm laser at 3.5 W/cm^2 for 15 min, the temperature increments are determined as 32.7, 37.5, 39.2, and 40.3 °C for the cupreous complexes with carboxylate-to-Cu(II) molar ratio of 1/1, 2/1, 3/1, and 4/1, respectively (Figure S5). CuCC NPs also exhibit good photothermal stability (Figure S6a,b). As irradiated by an 808 nm laser at 4 W/cm^2 for five cycles of heating−cooling, the change of absorption spectra and decrease of photothermal performance are hardly observed. In addition, because the formation of chitosan NPs strongly depends on the equilibrium of inter-NP electrostatic repulsion and inner-NP van der Waals attraction, the pH of NPs solution greatly influences the stability.[19,59] In our experiment, the stability of 44 nm NPs is poor out of the pH range of 3.0−4.0. The most favorable pH to keep CuCC NPs solution stable is 3.5. When the pH is lower than 3.0, the NPs will gradually fall apart due to acid-promoted chitosan dissolution. High dose of Cu(II) is detected by inductive coupled plasma (ICP), which indicates the release of cupreous complexes from NPs (Figure S7). As the pH is higher than 4.0, the NPs tend to aggregate within 3 d of storage, for example, in the aqueous solution of saline, phosphate buffered saline (PBS), cell culture, and the cell culture with 10% serum, due to the lack of electrostatic repulsion (Figure S6c). However, no huge dose of Cu(II) is detected (Figure S7). These evidence indicate that the dissolution of chitosan NPs is capable to promote the release of Cu(II), while NPs aggregation cannot.

To demonstrate the capability of CuCC NPs in photothermal therapy of cancer cells in vitro, the cytotoxicity is first tested for human oral epithelial carcinoma (KB) and squamous carcinoma (CAL-27) cells through a standard methyl thiazolyltetrozolium (MTT) assay after incubation with CuCC NPs for 24 h. The CuCC NPs possess relatively low toxicity for KB cells. As increasing NPs concentration to 400 μg/mL, the cell viability is still 80%. However, the NPs have a severe damage to CAL-27 cells. As the concentration gets to 100 μg/mL, the cell viability for CAL-27 cells is already down to 70%. Most of the cells are killed when the concentration reaches 400 μg/mL (Figure 4a). Consequently, KB cells are adopted for the further cell experiments because of the better biocompatibility with CuCC NPs. Note that pure cupreous complexes also exhibit severe cytotoxicity. 18.5 μg/mL cupreous complexes are toxic enough for killing most of the KB cells (Figure S8). It reveals that the embedment of cupreous complexes into polymer spheres can greatly suppress the release of inner toxicity.

The in vitro photothermal therapy is studied by comparing the viabilities of KB cells with 808 nm laser irradiation in the presence and absence of CuCC NPs. As increasing laser power density from 1 to 3 W/cm^2, KB cells after incubation with NPs are killed in growing proportion after 10 min irradiation. When the laser power density reaches 3 W/cm^2, the cell viability is lower than 30%, while the viability is almost 100% for the

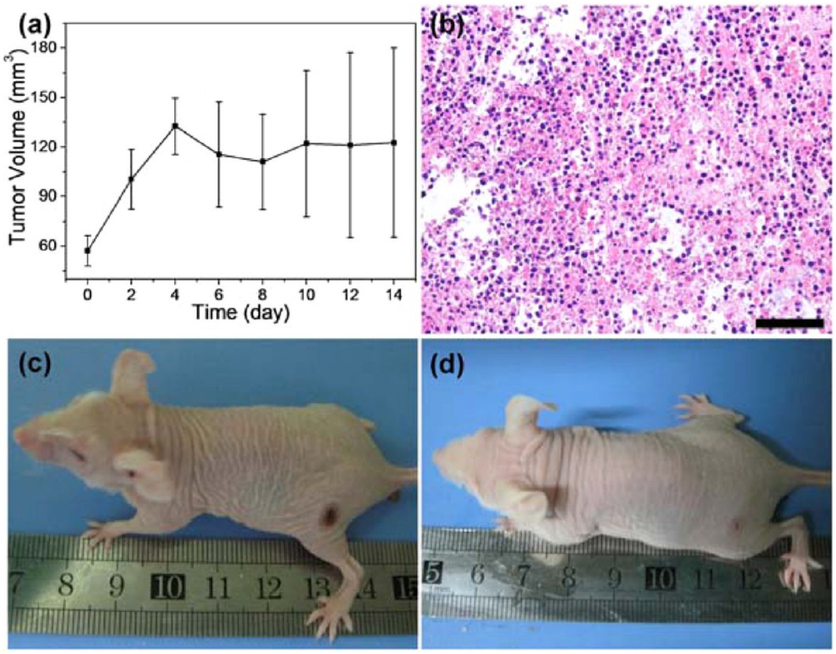

Figure 6. (a) The tumor volume change for NP only group. (b) H&E staining image of tumor from the photothermal therapy group the next day after treatment. The scale bar is 50 μm. Photographs of the mice after photothermal therapy for 0 (c) and 10 (d) days. The burned area heals gradually within 10 d.

control group without NPs incubation at this power density (Figure 4b). Additional propidium iodide (PI) fluorescent staining assay is also performed, which only stains apoptotic cells into red. As increasing the laser power density, an obvious increment of stained cells is found under dark field. When the power density reaches 3 W/cm^2, an aggregation of apoptotic cells is exhibited, which is one of the features of dead cells (Figure 4c-j). These results prove that CuCC NPs are workable for the photothermal therapy of cancer cells in vitro.

The in vivo photothermal test of CuCC NPs is further performed in nude mice bearing KB tumor models, because KB tumor is superficial and might be more suitable for clinical photothermal therapy than other tumors. The KB tumor models are subcutaneously implanted and divided into four groups. The growth and differentiation of tumors are fast (Figure 5a,c). Twenty days after implantation, the average tumor volumes reach 1800 mm^3 and weight in 1.24 g (the control group), taking up $\sim$5% body weight (Figure 5c,k). As for the mice without NPs injection but treated with 0.33 W/cm^2 808 nm laser for 12 min once every other day (the laser-only group), the tumors indicate slight depression in the first 8 d. However, in the following days, the tumors expand even faster than that of the control group (Figure 5a), and their average weight is 0.75 g (Figure 5d,l), which is attributed to the laser stimulus. In comparison, the tumors both injected with CuCC NPs and treated by laser irradiation (the photothermal therapy group) are ablated completely after the second treatment (Figure 5a,f).

In addition, the tumors from NP only group are also restrained greatly. An obvious inhibition of tumor volume is found since the fourth day after NP injection (Figure 6a). By the time tumors taken, the tumors show an average weight of 0.08 g, which are much smaller than those from the control group, and laser-only group (Figure 5e,m). The calculated tumor inhibition rate is 93.1%. This indicates the additional chemotherapeutic behavior of CuCC NPs, which is potential to solve the challenge of tumor reoccurrence.[34] Note that CuCC NPs exhibit low cytotoxicity within 24 h for KB cells (Figure 4a). No obvious inhibition is found until 4 d after injection. So, the high tumor inhibition rate should be resulted from the biodegradable chitosan using for loading CuCC NPs. The gradual degradation of chitosan allows the release of toxic cupreous complexes, poisoning the surrounding tumor tissue and restraining tumor growth. To prove the chemotherapeutic behavior of cupreous complexes, KB cells are incubated with different concentrations of cupreous complexes for 10 min, followed by PI staining. As increasing the concentration of cupreous complexes from 0 to 50 μg/mL, the increased cell apoptosis in red fluorescence is observed (Figure S9). Besides, the apoptotic cells turn into rotundity in comparison with the long-shaped healthy cells, which also exhibits the chemotherapeutic behavior of cupreous complexes. The chemotherapeutic behavior of CuCC NPs is further proved by hematoxylin−eosin (H&E) stained tumor slice, in which part of the tumor cells are damaged by the NPs (Figure 5i), while apoptosis is hardly observed from the control and laser-only groups (Figure 5g,h). The aforementioned results confirm that the chemotherapeutic behavior of CuCC NPs results from chitosan degradation and the subsequent release of cupreous complexes. Though chitosan degradation is not so fast in tumor environment (Figure 6a), there are effective ways to promote chitosan degradation, such as acid hydrolysis, oxidative degradation, radiation degradation, enzymatic degradation, and so forth. It indicates the hope to tune the release rate of cupreous complexes in further applications. Moreover, the additional chemotherapeutic behavior of CuCC NPs leads to synergistic effect, thus allowing to the complete tumor depression at the power density of 0.33 W/cm^2.

Furthermore, the tumors injected with CuCC NPs are destroyed completely after treated by 808 nm laser irradiation (Figure 5a,f), and no recrudesce is observed after 25 d. The burned skin recovers in the next 10 d (Figure 6c,d). From H&E

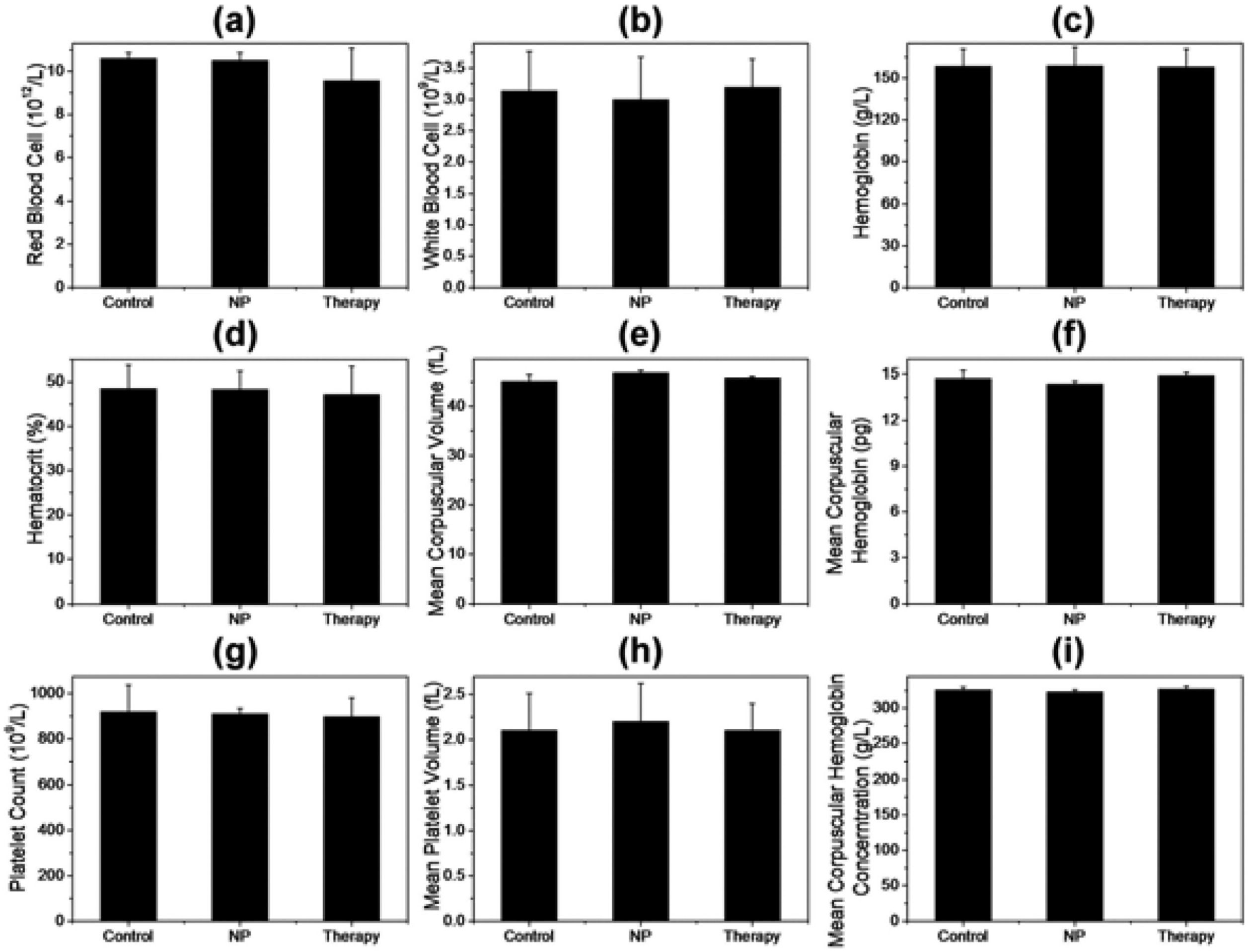

Figure 7. Blood analysis of mice after the injection of CuCC NPs for 30 d. (a) Red blood cells, (b) white blood cells, (c) hemoglobin, (d) hematocrit, (e) mean corpuscular volume, (f) mean corpuscular hemoglobin, (g) platelet count, (h) mean platelet volume, and (i) mean corpuscular hemoglobin concentration. No obvious difference is found between healthy and treated mice. The control group is age-matched healthy mice. The NP and therapy group refer to NP-only group and photothermal therapy group in our experiments.

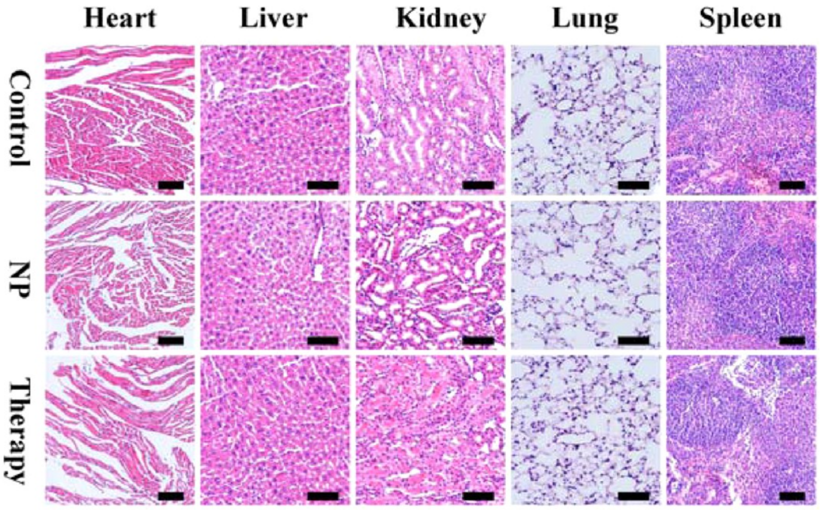

Figure 8. H&E stained splanchnic slices of heart, liver, kidney, lung, and spleen of mice after the injection of CuCC NPs for 16 d. No hydroncus or inflammatory cells are observed in the aforementioned organs. In comparison to the control group, the NP only and therapy groups have no difference. The control group is age-matched healthy mice. The NP and therapy group refer to NP-only group and photothermal therapy group in our experiments. The scale bar is 50 μm.

stained tumor slices for photothermal therapy group, a large area of damaged cancerous cells are observed immediately after laser treatment (Figure 5j). A complete damage is shown for the tumor taken 1 d after laser treatment (Figure 6b). The continuous damage to cancerous cells further confirms the role of CuCC NPs as chemotherapeutic agents to inhibit tumor recrudesce after photothermal therapy. Beside, the average body weight of each group is monitored (Figure 5b). A relative stable increase of body weight is observed for all groups in the first stage. But in the later stage, the change of body weights is different. The increase of body weights for the laser-only group is attributed to the expansion of tumors. For the control group, the mice suffer weight loss, while the tumors grow quickly. This indicates that KB tumors have already impeded the normal growth of mice. But for the NP only and photothermal therapy group, the body weights keep increasing, implying the recovery of mice after treatment (Figure 6d).

To investigate the long-term toxicity of CuCC NPs after therapy, a complete blood analysis including red blood cells, white blood cells, hemoglobin, hematocrit, mean corpuscular volume, mean corpuscular hemoglobin, platelet count, mean platelet volume, and mean corpuscular hemoglobin concentration are compared between NP only group, photothermal therapy group, and age-matched healthy mice (Figure 7). Though red and swollen is observed around the NP-treated areas (Figure 6c), and the ratio of neutrophilegranulocyte (NE) and lymphocyte (LY) in the white blood cell also shows slight inflammation after healing (Figure S10), all the parameters restore to normal level (Figure 7). In addition, H&E stained heart, liver, kidney, lung, and spleen do not show hydroncus or inflammatory cell infiltration, and the cells are basically at the same status compared with the healthy mice (Figure 8). These results indicate the safety of CuCC NPs as tumor therapeutic agents. In comparison to other photothermal agents, the CuCC NPs may not be as good as the plasmonic materials like Au nanorods and CuS NPs in heat supply due to the relatively lower light extinction ability. But the CuCC NPs can still accomplish complete tumor ablation under safe power density limitation through the synergistic effect of photothermal therapy and additional chemotherapy. Such synergistic effect makes CuCC NPs partially avoid the depth-dependent attenuation of laser intensity in deep tissue therapy, showing more potential in treating deep-seated tumors than plasmonic materials.

CONCLUSIONS

In summary, we demonstrate the facile and low-cost preparation of cupreous complexes-loaded chitosan NPs, which simultaneously exhibit photothermal therapeutic and chemotherapeutic behavior. The photothermal performance of cupreous complexes essentially results from the electrons transition between splitting Cu(II) d orbits, which is further enlarged as coordinating with carboxylate groups. As a result, the photothermal performance at NIR region is greatly enhanced, showing the photothermal transduction efficiency up to 60.3%. After loading cupreous complexes into chitosan and forming NPs, the improved biocompatibility assures the NPs as agents for photothermal therapy of KB cells in vitro and KB tumors in vivo. Since chitosan is biodegradable, the gradual release of cupreous complexes enables CuCC NPs as additional chemotherapeutic agents for KB tumors. The combination of photothermal therapy and chemotherapy of CuCC NPs makes these materials potential agents for noninvasive tumor ablation and for reducing the risk of postoperative recurrence.

EXPERIMENTAL SECTION

Materials. Poly(D-glucosamine) (chitosan) with medium molecular weight, 3-(4,5-dimethyl-2-thiazolyl)-2,5-diphenyl-2-*H*-tetrazolium bromide (MTT), and 3-mercaptopropionic acid (MPA, 99+%) were purchased from Sigma-Aldrich. Propidium iodide (PI) was purchased from Invitrogen. Analytical grade sodium hydroxide (NaOH), citrate acid monohydrate, cooper chloride dihydrate ($CuCl_2{\cdot}2H_2O$), and PBS were all commercially available products and used as received without further purification. Deionized water was used in all experiments.

Synthesis of CuCC Nanoparticles. Chitosan (5 mg), 24 mg of $CuCl_2$, and 56 mg of citric acid were dissolved in 40 mL of water. 1 M NaOH was used to adjust the pH value of mixtures to produce the NPs. pH was dominant for controlling the diameters of CuCC NPs from a few to thousands of nanometers. With the consideration of biological application, the pH was adjusted to 3.53 ± 0.5 to obtain the 44 nm NPs. The NPs were separated through centrifugation under 8000 r/min for 30 min. The cupreous complexes were prepared by mixing $CuCl_2$ and sodium citrate with specific ratio. Because each sodium citrate possesses three carboxylate groups, carboxylate-to-Cu(II) molar ratio is adopted to present the content of $CuCl_2$ and sodium citrate in cupreous complexes.

Cytotoxicity Assay and Photothermal Effect of CuCC Nanoparticles in Vitro. The 44 nm CuCC NPs were stable enough in the cytotoxicity assay, because they did not aggregate severely within 24 h due to the low concentration and short storage duration. So, no additional treatment was required in the following investigations. The human oral epithelial carcinoma (KB) cells and squamous cell carcinoma (CAL-27) cells were cultured in standard cell media. Cells were incubated with different concentrations of CuCC NPs and cupreous complexes for 24 h. The cell viability for KB and CAL-27 was evaluated by a standard methyl thiazolyl tetrozolium (MTT) assay on 96-well plates.[44] The optical density was measured at 490 nm for the MTT assay. As for the photothermal therapy in vitro, KB cells were incubated with 0.1 mg/mL CuCC NPs for 4 h, and then they were irradiated by an 808 nm NIR laser at different power density for 10 min. As for the control group, KB cells were not incubated with NPs but irradiated by laser at different power density. At last, MTT solution was added into the plates, and the cell viability was assumed by MTT assay. Each experiment was repeated five times.

Cell Uptake Efficiency. Thirty thousand KB cells were incubated in a 12-well plate with CuCC NPs feeding concentration of 100 μg/mL for 24 h. The cells were washed gently with saline three times to discard the excessive NPs and dissolved in aqua regia for determining Cu(II) content by ICP. For 44 nm CuCC NPs, the uptake efficiency was calculated as 37.9 ± 2.5%.

Propidium Iodide Stain Assay. For in vitro photothermal therapy, KB cells were first incubated with 0.1 mg/mL CuCC NPs for 4 h at the quantity of 30 000 cells per well on 6-well plates. Each plate was irradiated by an 808 nm NIR laser with different power density for 10 min. Subsequently, 0.001 mg/mL PI was added into the KB cell culture. After they were stained for 15 min, photos of cells were taken by a fluorescence microscope. To reveal the chemotherapeutic behavior of cupreous complexes, KB cells were incubated with different concentrations of cupreous complexes for 10 min and stained with 0.001 mg/mL PI for 15 min.

Animal Experiments. Thirty BALB/c-nu mice of 4−6 weeks old were purchased from Beijing Huafukang Biological Technology Co. Ltd. and used under protocols approved by Jilin University Laboratory Animal Center. After one week's observation and their weights got heavier than 22 g, 1.5×10^6 of KB cells dispersed in 150 μL of cell culture were injected subcutaneously into the left back leg. The average tumor size reached ~60 mm^3 in 6 d, and the tumor formation ratio was 93.3%. The 28 mice with tumor models were divided into four groups: control group, laser-only group, NP-only group, and photothermal therapy group. The latter two groups were injected with 50 μL of 2 mg/mL CuCC NPs in 9% saline, while the former two groups were only injected with 50 μL of saline at the center of the tumor. The NPs were administered through intratumoral injection. After the injection of NPs, the tumor volume expanded immediately by forming a bubble, which made it incorrect to monitor the alteration of tumor volume in photothermal therapy. So, laser was applied 2 d later to ensure the absorption of the bubble. Two days later, the laser-only group and therapy group were irradiated at the density of 0.33 W/cm^2 for 12 min with consideration of the safety limitation of 808 nm laser according to the American National Standards Institute Laser Safety Standards. In addition, tumor sizes and mouse weights were recorded every other day. The tumor volume V (mm^3) was estimated by the following formula:

$$V = \frac{1}{2}L \times D^2 \qquad (4)$$

where L and D (mm) represented the lengths of long and short axes, respectively.

The tumor size expands dramatically, especially for the control group. Except for the photothermal therapy group, five mice in each group were killed through spine dislocation, and tumors were taken, weighted, and photographed in the 16th day. Then tumors were marinated in formalin for histological sections. The H&E staining was performed. For the photothermal therapy group, one of the tumors was taken immediately after laser treatment, and the next day another tumor was taken for H&E staining to monitor the cells in the damaged area. The other mice in each group were reserved for routine blood test and heart perfusion. The viscera including lungs, liver, heart, spleen, and kidneys were taken and stored in formalin for H&E staining.

Characterization. UV−visible absorption spectra were obtained using a UV-3600 UV−vis spectrophotometer at room temperature under ambient conditions. Transmission electron microscopy was conducted using a Hitachi H-800 electron microscope at an acceleration voltage of 200 kV with a CCD camera. Dynamic light scattering measurements were performed using a Zetasizer NanoZS (Malvern Instruments). Inductive coupled plasma emission spectrometer was performed with Perkin Elmer Optima 3300DV analyzer. In the study of photothermal effect, an 808 nm diode laser (LEO photonics Co. Ltd.) was employed with the output power tunable from 0 to 10 W/cm^2. The temperature increment under laser irradiation was determined by an electric thermometer (Traceable Callbraion, 0.1 °C). Solution (2.0 mL) was added into 1 × 1 × 4 cm quartz pool with tinfoil capped to prevent the vaporization of water and irradiated by 808 nm laser at various power densities. The variation of the temperature was immediately measured after irradiation. The concentration effect was studied by diluting the CuCC NPs and cupreous complexes to specific concentrations. The output power and irradiation duration was fixed at 3.5 W/cm^2 and 15 min, respectively. The effect of output power was revealed by irradiating the CuCC NPs and cupreous complexes with specific output power density for 15 min. Thermogravimetric analysis was measured on an American TA Q500 analyzer under N_2 atmosphere with the flow rate of 100 mL·min^{-1}. Before TGA measurement, the samples were dried at 100 °C for 1 h. Bright field and fluorescent images of KB cells were obtained by an Olympus IX71 inverted fluorescence microscope.

■ ASSOCIATED CONTENT

Ⓢ Supporting Information

The Supporting Information is available free of charge on the ACS Publications website at DOI: 10.1021/acsami.5b05866.

> Additional structural characterizations by FTIR, photothermal performance, TGA curves, colloidal stability, calculations, and toxicity of cupreous complexes and CuCC NPs. (PDF)

■ AUTHOR INFORMATION

Corresponding Authors

*Fax: +86 431 85193423. E-mail: hao_zhang@jlu.edu.cn. (H.Z.)
*E-mail: hcsun@mail.jlu.edu.cn. (H.-C.S.)
*E-mail: daqizhang@yeah.net. (D.Z.)

Author Contributions

The manuscript was written through contributions of all authors. All authors have given approval to the final version of the manuscript.

Notes

The authors declare no competing financial interest.

■ ACKNOWLEDGMENTS

This work was supported by NSFC (51425303, 21374042, 21174051, 21221063, 81320108011), the 973 Program of China (2014CB643503), Natural Science Foundation of Jilin Province (20140101048JC), the Special Project from MOST of China, and the Fundamental Research Funds for the Central Universities.

■ REFERENCES

(1) Sun, T.; Zhang, Y. S.; Pang, B.; Hyun, D. C.; Yang, M.; Xia, Y. Engineered Nanoparticles for Drug Delivery in Cancer Therapy. *Angew. Chem., Int. Ed.* **2014**, *53*, 12320−12364.

(2) Huang, P.; Lin, J.; Li, W.; Rong, P.; Wang, Z.; Wang, S.; Wang, X.; Sun, X.; Aronova, M.; Niu, G.; Leapman, R. D.; Nie, Z.; Chen, X. Biodegradable Gold Nanovesicles with an Ultrastrong Plasmonic Coupling Effect for Photoacoustic Imaging and Photothermal Therapy. *Angew. Chem., Int. Ed.* **2013**, *52*, 13958−13964.

(3) Melamed, J. R.; Edelstein, R. S.; Day, E. S. Elucidating the Fundamental Mechanisms of Cell Death Triggered by Photothermal Therapy. *ACS Nano* **2015**, *9*, 6−11.

(4) Han, B.; Zhu, Z.; Li, Z.; Zhang, W.; Tang, Z. Conformation Modulated Optical Activity Enhancement in Chiral Cysteine and Au Nanorod Assemblies. *J. Am. Chem. Soc.* **2014**, *136*, 16104−16107.

(5) Chen, M.; Tang, S.; Guo, Z.; Wang, X.; Mo, S.; Huang, X.; Liu, G.; Zheng, N. Core−Shell Pd@Au Nanoplates as Theranostic Agents for *in-Vivo* Photoacoustic Imaging, CT Imaging, and Photothermal Therapy. *Adv. Mater.* **2014**, *26*, 8210−8216.

(6) Mahmoudi, M.; Lohse, S. E.; Murphy, C. J.; Fathizadeh, A.; Montazeri, A.; Suslick, K. S. Variation of Protein Corona Composition of Gold Nanoparticles Following Plasmonic Heating. *Nano Lett.* **2014**, *14*, 6−12.

(7) Ding, X.; Liow, C. H.; Zhang, M.; Huang, R.; Li, C.; Shen, H.; Liu, M.; Zou, Y.; Gao, N.; Zhang, Z.; Li, Y.; Wang, Q.; Li, S.; Jiang, J. Surface Plasmon Resonance Enhanced Light Absorption and Photothermal Therapy in the Second Near-Infrared Window. *J. Am. Chem. Soc.* **2014**, *136*, 15684−15693.

(8) Li, B.; Ye, K.; Zhang, Y.; Qin, J.; Zou, R.; Xu, K.; Huang, X.; Xiao, Z.; Zhang, W.; Lu, X.; Hu, J. Photothermal Theragnosis Synergistic Therapy Based on Bimetal Sulphide Nanocrystals Rather Than Nanocomposites. *Adv. Mater.* **2015**, *27*, 1339−1345.

(9) Chen, Q.; Liang, C.; Wang, C.; Liu, Z. An Imagable and Photothermal "Abraxane-Like" Nanodrug for Combination Cancer Therapy to Treat Subcutaneous and Metastatic Breast Tumors. *Adv. Mater.* **2015**, *27*, 903−910.

(10) Vijayaraghavan, P.; Liu, C.-H.; Vankayala, R.; Chiang, C.-S.; Hwang, K. C. Designing Multi-Branched Gold Nanoechinus for NIR Light Activated Dual Modal Photodynamic and Photothermal Therapy in the Second Biological Window. *Adv. Mater.* **2014**, *26*, 6689−6695.

(11) Zhang, Z.; Wang, J.; Chen, C. Near-Infrared Light-Mediated Nanoplatforms for Cancer Thermo-Chemotherapy and Optical Imaging. *Adv. Mater.* **2013**, *25*, 3869−3880.

(12) Lee, G. Y.; Qian, W. P.; Wang, L.; Wang, Y. A.; Staley, C. A.; Satpathy, M.; Nie, S.; Mao, H.; Yang, L. Theranostic Nanoparticles with Controlled Release of Gemcitabine for Targeted Therapy and MRI of Pancreatic Cancer. *ACS Nano* **2013**, *7*, 2078−2089.

(13) Yang, Y.; Liu, X.; Lv, Y.; Herng, T. S.; Xu, X.; Xia, W.; Zhang, T.; Fang, J.; Xiao, W.; Ding, J. Orientation Mediated Enhancement on

Magnetic Hyperthermia of Fe_3O_4 Nanodisc. *Adv. Funct. Mater.* **2015**, *25*, 812−820.

(14) Liu, J.; Zheng, X.; Yan, L.; Zhou, L.; Tian, G.; Yin, W.; Wang, L.; Liu, Y.; Hu, Z.; Gu, Z.; Chen, C.; Zhao, Y. Bismuth Sulfide Nanorods as a Precision Nanomedicine for *in Vivo* Multimodal Imaging-Guided Photothermal Therapy of Tumor. *ACS Nano* **2015**, *9*, 696−707.

(15) Lazarovits, J.; Chen, Y. Y.; Sykes, E. A.; Chan, W. C. W. Nanoparticle-Blood Interactions: The Implications on Solid Tumour Targeting. *Chem. Commun.* **2015**, *51*, 2756−2767.

(16) Zhang, P.; He, Z.; Wang, C.; Chen, J.; Zhao, J.; Zhu, X.; Li, C.-Z.; Min, Q.; Zhu, J.-J. *In Situ* Amplification of Intracellular MicroRNA with MNAzyme Nanodevices for Multiplexed Imaging, Logic Operation, and Controlled Drug Release. *ACS Nano* **2015**, *9*, 789−798.

(17) Xiao, Z.; Ji, C.; Shi, J.; Pridgen, E. M.; Frieder, J.; Wu, J.; Farokhzad, O. C. DNA Self-Assembly of Targeted Near-Infrared-Responsive Gold Nanoparticles for Cancer Thermo-Chemotherapy. *Angew. Chem., Int. Ed.* **2012**, *51*, 11853−11857.

(18) Shanmugam, V.; Chien, Y.-H.; Cheng, Y.-S.; Liu, T.-Y.; Huang, C.-C.; Su, C.-H.; Chen, Y.-S.; Kumar, U.; Hsu, H.-F.; Yeh, C.-S. Oligonucleotides-Assembled Au Nanorod-Assisted Cancer Photothermal Ablation and Combination Chemotherapy with Targeted Dual-Drug Delivery of Doxorubicin and Cisplatin Prodrug. *ACS Appl. Mater. Interfaces* **2014**, *6*, 4382−4393.

(19) Guo, L.; Yan, D. D.; Yang, D.; Li, Y.; Wang, X.; Zalewski, O.; Yan, B.; Lu, W. Combinatorial Photothermal and Immuno Cancer Therapy Using Chitosan-Coated Hollow Copper Sulfide Nanoparticles. *ACS Nano* **2014**, *8*, 5670−5681.

(20) Rengan, A. K.; Bukhari, A. B.; Pradhan, A.; Malhotra, R.; Banerjee, R.; Srivastava, R.; De, A. *In Vivo* Analysis of Biodegradable Liposome Gold Nanoparticles as Efficient Agents for Photothermal Therapy of Cancer. *Nano Lett.* **2015**, *15*, 842−848.

(21) Wang, S.; Riedinger, A.; Li, H.; Fu, C.; Liu, H.; Li, L.; Liu, T.; Tan, L.; Barthel, M. J.; Pugliese, G.; de Donato, F.; D'Abbusco, M. S.; Meng, X.; Manna, L.; Meng, H.; Pellegrino, T. Plasmonic Copper Sulfide Nanocrystals Exhibiting Near-Infrared Photothermal and Photodynamic Therapeutic Effects. *ACS Nano* **2015**, *9*, 1788−1800.

(22) Tian, Q.; Wang, Q.; Yao, K. X.; Teng, B.; Zhang, J.; Yang, S.; Han, Y. Multifunctional Polypyrrole@Fe_3O_4 Nanoparticles for Dual-Modal Imaging and *in Vivo* Photothermal Cancer Therapy. *Small* **2014**, *10*, 1063−1068.

(23) Wang, D.; Fei, B.; Halig, L. V.; Qin, X.; Hu, Z.; Xu, H.; Wang, Y. A.; Chen, Z.; Kim, S.; Shin, D. M.; Chen, Z. Targeted Iron-Oxide Nanoparticle for Photodynamic Therapy and Imaging of Head and Neck Cancer. *ACS Nano* **2014**, *8*, 6620−6632.

(24) Wang, H.; Mararenko, A.; Cao, G.; Gai, Z.; Hong, K.; Banerjee, P.; Zhou, S. Multifunctional 1D Magnetic and Fluorescent Nanoparticle Chains for Enhanced MRI, Fluorescent Cell Imaging, and Combined Photothermal/Chemotherapy. *ACS Appl. Mater. Interfaces* **2014**, *6*, 15309−15317.

(25) Hembury, M.; Chiappini, C.; Bertazzo, S.; Kalber, T. L.; Drisko, G. L.; Ogunlade, O.; Walker-Samuel, S.; Krishna, K. S.; Jumeaux, C.; Beard, P.; Kumar, C. S. S. R.; Porter, A. E.; Lythgoe, M. F.; Boissière, C.; Sanchez, C.; Stevens, M. M. Gold−Silica Quantum Rattles for Multimodal Imaging and Therapy. *Proc. Natl. Acad. Sci. U. S. A.* **2015**, *112*, 1959−1964.

(26) Brongersma, M. L.; Halas, N. J.; Nordlander, P. Plasmon-Induced Hot Carrier Science and Technology. *Nat. Nanotechnol.* **2015**, *10*, 25−34.

(27) Yang, J.; Choi, J.; Bang, D.; Kim, E.; Lim, E.-K.; Park, H.; Suh, J.-S.; Lee, K.; Yoo, K.-H.; Kim, E.-K.; Huh, Y.-M.; Haam, S. Convertible Organic Nanoparticles for Near-Infrared Photothermal Ablation of Cancer Cells. *Angew. Chem., Int. Ed.* **2011**, *50*, 441−444.

(28) Jiang, N.; Shao, L.; Wang, J. (Gold Nanorod Core)/(Polyaniline Shell) Plasmonic Switches with Large Plasmon Shifts and Modulation Depths. *Adv. Mater.* **2014**, *26*, 3282−3289.

(29) Pérez-Hernández, M.; del Pino, P.; Mitchell, S. G.; Moros, M.; Stepien, G.; Pelaz, B.; Parak, W. J.; Gálvez, E. M.; Pardo, J.; de la Fuente, J. M. Dissecting the Molecular Mechanism of Apoptosis during Photothermal Therapy Using Gold Nanoprisms. *ACS Nano* **2015**, *9*, 52−61.

(30) Liu, K.; Nie, Z.; Zhao, N.; Li, W.; Rubinstein, M.; Kumacheva, E. Step-Growth Polymerization of Inorganic Nanoparticles. *Science* **2010**, *329*, 197−200.

(31) Goodman, A. M.; Cao, Y.; Urban, C.; Neumann, O.; Ayala-Orozco, C.; Knight, M. W.; Joshi, A.; Nordlander, P.; Halas, N. J. The Surprising *in Vivo* Instability of Near-IR-Absorbing Hollow Au-Ag Nanoshells. *ACS Nano* **2014**, *8*, 3222−3231.

(32) Zhang, C.-L.; Lv, K.-P.; Cong, H.-P.; Yu, S.-H. Controlled Assemblies of Gold Nanorods in PVA Nanofiber Matrix as Flexible Free-Standing SERS Substrates by Electrospinning. *Small* **2012**, *8*, 648−653.

(33) Mooney, R.; Roma, L.; Zhao, D.; van Haute, D.; Garcia, E.; Kim, S. U.; Annala, A. J.; Aboody, K. S.; Berlin, J. M. Neural Stem Cell-Mediated Intratumoral Delivery of Gold Nanorods Improves Photothermal Therapy. *ACS Nano* **2014**, *8*, 12450−12460.

(34) Ayala-Orozco, C.; Urban, C.; Knight, M. W.; Urban, A. S.; Neumann, O.; Bishnoi, S. W.; Mukherjee, S.; Goodman, A. M.; Charron, H.; Mitchell, T.; Shea, M.; Roy, R.; Nanda, S.; Schiff, R.; Halas, N. J.; Joshi, A. Au Nanomatryoshkas as Efficient Near-Infrared Photothermal Transducers for Cancer Treatment: Benchmarking against Nanoshells. *ACS Nano* **2014**, *8*, 6372−6381.

(35) Lee, S.-M.; Kim, H. J.; Ha, Y.-J.; Park, Y. N.; Lee, S.-K.; Park, Y.-B.; Yoo, K.-H. Targeted Chemo-Photothermal Treatments of Rheumatoid Arthritis Using Gold Half-Shell Multifunctional Nanoparticles. *ACS Nano* **2013**, *7*, 50−57.

(36) Chirico, G.; Pallavicini, P.; Collini, M. Gold Nanostars for Superficial Diseases: A Promising Tool for Localized Hyperthermia? *Nanomedicine* **2014**, *9*, 1−3.

(37) Yuan, H.; Fales, A. M.; Vo-Dinh, T. TAT Peptide-Functionalized Gold Nanostars: Enhanced Intracellular Delivery and Efficient NIR Photothermal Therapy Using Ultralow Irradiance. *J. Am. Chem. Soc.* **2012**, *134*, 11358−11361.

(38) Shi, P.; Liu, Z.; Dong, K.; Ju, E.; Ren, J.; Du, Y.; Li, Z.; Qu, X. A Smart "Sense-Act-Treat" System: Combining a Ratiometric pH Sensor with a Near Infrared Therapeutic Gold Nanocage. *Adv. Mater.* **2014**, *26*, 6635−6641.

(39) Lee, U. Y.; Youn, Y. S.; Park, J.; Lee, E. S. Y-Shaped Ligand-Driven Gold Nanoparticles for Highly Efficient Tumoral Uptake and Photothermal Ablation. *ACS Nano* **2014**, *8*, 12858−12865.

(40) Lohse, S. E.; Murphy, C. J. The Quest for Shape Control: A History of Gold Nanorod Synthesis. *Chem. Mater.* **2013**, *25*, 1250−1261.

(41) Sau, T. K.; Rogach, A. L. Nonspherical Noble Metal Nanoparticles: Colloid-Chemical Synthesis and Morphology Control. *Adv. Mater.* **2010**, *22*, 1781−1804.

(42) An, F.-F.; Deng, Z.-J.; Ye, J.; Zhang, J.-F.; Yang, Y.-L.; Li, C.-H.; Zheng, C.-J.; Zhang, X.-H. Aggregation-Induced Near-Infrared Absorption of Squaraine Dye in an Albumin Nanocomplex for Photoacoustic Tomography. *ACS Appl. Mater. Interfaces* **2014**, *6*, 17985−17992.

(43) Wang, Y.; Wang, K.; Zhao, J.; Liu, X.; Bu, J.; Yan, X.; Huang, R. Multifunctional Mesoporous Silica-Coated Graphene Nanosheet Used for Chemo-Photothermal Synergistic Targeted Therapy of Glioma. *J. Am. Chem. Soc.* **2013**, *135*, 4799−4804.

(44) Liang, X.; Li, X.; Jing, L.; Yue, X.; Dai, Z. Theranostic Porphyrin Dyad Nanoparticles for Magnetic Resonance Imaging Guided Photodynamic Therapy. *Biomaterials* **2014**, *35*, 6379−6388.

(45) Nair, L. V.; Nagaoka, Y.; Maekawa, T.; Sakthikumar, D.; Jayasree, R. S. Quantum Dot Tailored to Single Wall Carbon Nanotubes: A Multifunctional Hybrid Nanoconstruct for Cellular Imaging and Targeted Photothermal Therapy. *Small* **2014**, *10*, 2771−2775.

(46) Feng, W.; Zhou, X.; Nie, W.; Chen, L.; Qiu, K.; Zhang, Y.; He, C. Au/Polypyrrole@Fe_3O_4 Nanocomposites for MR/CT Dual-Modal Imaging Guided-Photothermal Therapy: An *in Vitro* Study. *ACS Appl. Mater. Interfaces* **2015**, *7*, 4354−4367.

(47) Reátegui, E.; Aceto, N.; Lim, E. J.; Sullivan, J. P.; Jensen, A. E.; Zeinali, M.; Martel, J. M.; Aranyosi, A. J.; Li, W.; Castleberry, S.; Bardia, A.; Sequist, L. V.; Haber, D. A.; Maheswaran, S.; Hammond, P. T.; Toner, M.; Stott, S. L. Tunable Nanostructured Coating for the Capture and Selective Release of Viable Circulating Tumor Cells. *Adv. Mater.* **2015**, *27*, 1593−1599.

(48) Fujie, T.; Mori, Y.; Ito, S.; Nishizawa, M.; Bae, H.; Nagai, N.; Onami, H.; Abe, T.; Khademhosseini, A.; Kaji, H. Micropatterned Polymeric Nanosheets for Local Delivery of an Engineered Epithelial Monolayer. *Adv. Mater.* **2014**, *26*, 1699−1705.

(49) Gan, Z.; Wu, X.; Meng, M.; Zhu, X.; Yang, L.; Chu, P. K. Photothermal Contribution to Enhanced Photocatalytic Performance of Graphene-Based Nanocomposites. *ACS Nano* **2014**, *8*, 9304−9310.

(50) Jung, H. S.; Kong, W. H.; Sung, D. K.; Lee, M.-Y.; Beack, S. E.; Keum, D. H.; Kim, K. S.; Yun, S. H.; Hahn, S. K. Nanographene OxideHyaluronic Acid Conjugate for Photothermal Ablation Therapy of Skin Cancer. *ACS Nano* **2014**, *8*, 260−268.

(51) Creighton, J. A.; Eadon, D. G. Ultraviolet-Visible Absorption Spectra of the Colloidal Metallic Elements. *J. Chem. Soc., Faraday Trans.* **1991**, *87*, 3881−3891.

(52) Mack, J.; Stillman, M. J. Transition Assignments in the Ultraviolet-Visible Absorption and Magnetic Circular Dichroism Spectra of Phthalocyanines. *Inorg. Chem.* **2001**, *40*, 812−814.

(53) Li, W.-K.; Zhou, G.-D.; Mak, T. C. W. *Advanced Structural Inorganic Chemistry;* Oxford University Press: Oxford, U.K., 2008; Chapter 8.3.

(54) Augustyniak, M. A.; Usachev, A. E. The Host Lattice Influence on the Jahn-Teller Effect of the $Cu(H_2O)_6^{2+}$ Complex Studied by EPR in $K_2Zn(SO_4)_2·6H_2O$ and $(NH_4)_2Zn(SO_4)_2·6H_2O$ Tutton Salt Crystals. *J. Phys.: Condens. Matter* **1999**, *11*, 4391−4400.

(55) Zhou, J.; Duan, B.; Fang, Z.; Song, J.; Wang, C.; Messersmith, P. B.; Duan, H. Interfacial Assembly of Mussel-Inspired Au@Ag@ Polydopamine Core−Shell Nanoparticles for Recyclable Nanocatalysts. *Adv. Mater.* **2014**, *26*, 701−705.

(56) Li, C.; Chen, T.; Ocsoy, I.; Zhu, G.; Yasun, E.; You, M.; Wu, C.; Zheng, J.; Song, E.; Huang, C. Z.; Tan, W. Gold-Coated Fe_3O_4 Nanoroses with Five Unique Functions for Cancer Cell Targeting, Imaging, and Therapy. *Adv. Funct. Mater.* **2014**, *24*, 1772−1780.

(57) Lin, L.-S.; Cong, Z.-X.; Cao, J.-B.; Ke, K.-M.; Peng, Q.-L.; Gao, J.; Yang, H.-H.; Liu, G.; Chen, X. Multifunctional Fe_3O_4@Polydopamine CoreShell Nanocomposites for Intracellular mRNA Detection and Imaging-Guided Photothermal Therapy. *ACS Nano* **2014**, *8*, 3876−3883.

(58) Bai, J.; Liu, Y.; Jiang, X. Multifunctional PEG-GO/CuS Nanocomposites for Near-Infrared Chemo-Photothermal Therapy. *Biomaterials* **2014**, *35*, 5805−5813.

(59) Mallick, S.; Sharma, S.; Banerjee, M.; Ghosh, S. S.; Chattopadhyay, A.; Paul, A. Iodine-Stabilized Cu Nanoparticle Chitosan Composite for Antibacterial Applications. *ACS Appl. Mater. Interfaces* **2012**, *4*, 1313−1323.

DOI: 10.1021/acsami.5b05866
ACS Appl. Mater. Interfaces 2015, 7, 20801−20812